Hindawi
Advances in Civil Engineering
Volume 2018, Article ID 2837571, 9 pages
https://doi.org/10.1155/2018/2837571

Research Article

Microscopic Parameter Extraction and Corresponding Strength Prediction of Cemented Paste Backfill at Different Curing Times

Xuebin Qin, Lang Liu, Pai Wang, Mei Wang, and Jie Xin

Xi'an University of Science and Technology, 58 Yanta Rd., Xi'an, Shaanxi, China

Correspondence should be addressed to Xuebin Qin; qinxb@xust.edu.cn

Received 22 February 2018; Accepted 18 April 2018; Published 27 May 2018

Academic Editor: Yixian Wang

To accurately and intuitively study the influence of microscopic parameters and mechanical responses of the consolidation process of cemented paste backfill (CPB), a method is proposed for characterizing its geometric and morphological characteristics and its mechanical response. A set of microstructure parameter software is developed for analyzing the CPB consolidation process, which quantitatively analyzes the mechanical response of CPBs at a microscopic scale. Based on the fuzzy clustering method, CPB microscopic pore images are extracted via digital image processing technology. Microscopic CPB pores are extracted from images via cluster analysis, binarization, and denoising techniques. Then, images are evaluated for porosity, number of pores, average pore width, fractal dimension, weighted probability entropy, and 11 more indicators to quantitatively analyze pores. Thus, the proposed method forms nonlinear relationships between microstructure parameters and mechanical responses based on a deep learning TensorFlow framework under different curing times. Results show that the multiparameter predictive mechanical response at the microscopic scale has a good effect, and the predicted average error is 9.51%. The accuracy of the proposed method is higher than that of the traditional method. Therefore, the proposed method provides a new method to quantitatively analyze the mechanical response strength prediction at a microscale.

1. Introduction

Owing to the gradual depletion of mineral resources in the shallow parts of the Earth, deep mineral resource mining has become commonplace and increasingly important. The strength of the backfill material is critical. Based on the strength characteristics of cemented paste backfill (CPB) at high altitudes, Gan Deqing et al., from the North China University of Science and Technology, analyzed CPB strength from the macroscopic and microscopic perspectives. By comparing and analyzing CPBs under different curing conditions, they learned that strengths differ according to the law of increasing backfill strength [1]. Xin and Bingwen, from the China University of Mining and Technology, established a relationship between the CPB's macroscopic mechanical properties and the type and quantity of hydration products of cementitious materials, using a series of research methods, including X-ray diffractometry, thermogravimetry and differential scanning calorimetry, and scanning electron microscopy (SEM) [2]. Qinli et al., of Central South University, optimized the CPB ratio by using a neural network, which took the concentration of slurry and the amount of each component as input. The respective slump measures of compression strength at 7 and 28 days were regarded as output factors, and the matching experimental data for training and testing samples were established using a back propagation neural network prediction model [3]. Jianxin et al. designed a single-factor, five-level (i.e., CPB strength, solid content, ratio of lime to sand, curing time, and strength sensitivity and failure mechanism) experiment, using cement to make the CPB [4]. Fall et al. studied the effects of curing temperatures for CPB strength [5]. Professor Wenbin et al., at the China University of Mining and Technology, studied the

Table 1: Basic physical properties of tailing.

Sample	Proportion (t/m^3)	Bulk density (t/m^3)		Stacking density		Porosity (%)	
		Loose	Dense	Loose	Dense	Loose	Dense
Tailings	2.852	1.229	1.545	0.431	0.542	56.92	45.82

law of stress-strain variation, electrical resistivity, and CPB temperature during uniaxial compression, analyzing the precursory characteristics of failure and instability. They also compared the sensitivity and variability of monitoring information about the same failures, and overcame low confidence levels, high error rates, and so on, of the prediction method by only considering the variation of one parameter [6–8]. Sun et al. obtained the multicomponent 3D structure and porosity value using real-time 3D reconstruction of a CT scan image of a CPB sample, simulating crack propagation and stress variation of the sample using the discrete element method [9]. Xiu et al. revealed the microscopic tailing chemical reaction mechanism and studied the macroscopic effects of CPB stability by conducting experiments under different tailing mixture ratios [10]. Liu et al. obtained the basic parameters of pore images, including porosity and fractal dimension, by means of manual thresholds on a single SEM image. They analyzed the relationship between the microscopic structure and the mechanical strength of rock [11, 12]. Outllet et al. analyzed the pore structures of CPB samples using SEM images, estimating the structural parameters of pores by measuring total porosity, pore size distribution, and pore space curvature [13]. Neural network is used to predict concrete compressive strength [14, 15]. Momeni et al. predicted uniaxial compressive strength of a rock sample using hybrid particle swarm optimization [16]. Nicola et al. proposed peak strength and ultimate strain prediction for FRP-confined square and circular concrete sections [17]. Therefore, extensive research exists about mechanical strength prediction in fields, including rock mechanics and CPBs. However, there is little research on the automatic prediction of mechanical responses in CPB using image processing methods on a microscopic scale.

This paper summarizes studies of CPBs at different curing times and characterizes the geometrical characteristics and morphological structures of the pore network based on measuring indexes, such as number of pores, total area of pores, maximum area of pores, average area of pores, average length of long axis, porosity, coefficient of uniformity, sorting coefficient, curvature coefficient, fractal dimension, and weighted probability entropy, by conducting indoor microscopic tests and extracting the microscopic pore images using an image processing technique. This paper analyzes the effects of the CPB microscopic parameters on the mechanical response strength, using a slurry concentration of 72% and a cement-sand ratio of 1 : 4 at different curing times. A visual quantification method is offered for analyzing the relationship between the pore structure and the mechanical response of the CPB during solidification on a microscopic scale.

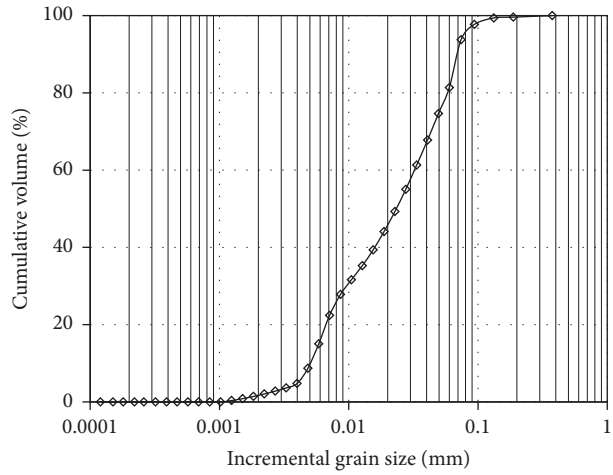

Figure 1: Distribution curve for grain sizes of tailings.

Table 2: Test design plan.

Slurry concentration (%)	Gelling agent	Cement-sand ratio
72	OPC	1 : 4

2. Materials and Test Methods

2.1. Material Components. Tailing is used during testing to analyze basic performance. The primary physical properties of the determination results are shown in Table 1. The particle size distribution curve is shown in Figure 1. The gel material is common silicate cement, and the test water is urban tap water. In Figure 1, tailings of d_{10}, d_{30}, and d_{60} have grain sizes of 4.96 μm, 10.02 μm, and 32.29 μm, respectively. The tailing grain size composition coefficient of uniformity is 6.46. The optimal gradation of tailing particles complied with the Thabo equation generally ranges from 4 to 6. The tailing grain size curve reveals that the test tailing has a low proportion of coarse particles because of its natural gradation being classified as a relative gap gradation.

2.2. Test Process

2.2.1. Sample Preparation. Four identical samples are fabricated simultaneously, one as standby and the other three as test samples. As per the experimental design plan summarized in Table 2, the mass of common silicate cement is computed using the cement-sand ratio. Then, the cement is weighed. Using the mixture ratio shown in Table 4, the tailing and cement are weighed and well mixed. The tap water is added for proper preparation of samples, giving a slurry mass ratio of 72%. The sample is manually stirred for

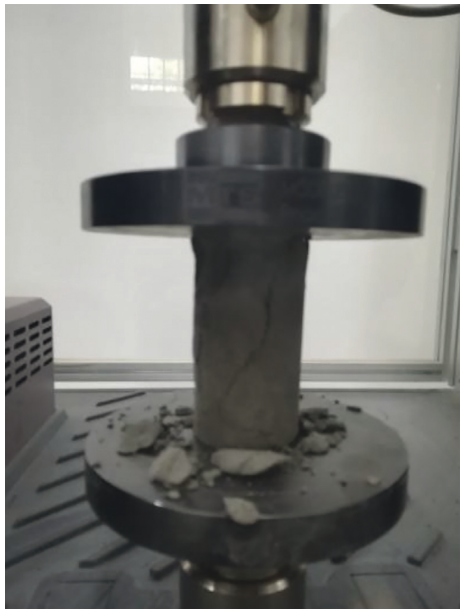

Figure 2: Uniaxial compressive strength test of cemented tailings backfill.

5 min until the CPB is well mixed. A layer of Vaseline is applied to the circular cast iron test mold having a diameter of 50 mm and a height of 100 mm. The CPB is loaded in the test mold in three layers. Each layer is then compacted by vibration. The CPB is then allowed to remain still for 24 h after being loaded. The surface of the test sample is then smoothed by scraping, and the mold is removed. The test samples are properly labeled and placed in a constant-temperature, constant-humidity curing box at a temperature of $(20 \pm 1)^{\circ}$C and a humidity of (95 ± 1) %.

2.2.2. Test of Uniaxial Compressive Strength. Each test sample is removed and measured for height and diameter with a Vernier caliper at 3, 7, 14, 28, and 56 days after curing. A computer-controlled 20 kN pressure machine is used to apply pressure at a constant rate of 1 mm/min until the test sample fails, as shown in Figure 2. The data are then collated to compute the test pieces' uniaxial compressive strengths, which are then averaged to obtain the result.

2.3. Preparation of SEM Samples. SEM samples are created during the research. As a modern detection technology, a SEM is characterized by high resolution, large magnification time, wide field-of-view, strong effects of 3D images, and so on. Consequently, samples are required to be dried and gilded to obtain a true and clear observation.

The CPB is selected at different curing times for preparation of the SEM test samples. First, we locate the middle part of the cement backfill and use a double-sided blade wire saw coated with Vaseline to cut a 10 mm × 10 mm × 10 mm roughcast cube with 1.5 mm border. A sharp backfill paste steel knife is then used to cut the blank and create a fresh cross section, baring a complete natural structural surface. This is then cut into a 5 mm × 5 mm × 5 mm block for observation under the electron microscope. For this, the fresh surface should be as flat as possible with all disturbance particles removed by a rubber suction bulb.

3. Extraction of Microscopic Pore Images and Quantitative Analysis

Authors should discuss the results and how they can be interpreted in perspective of previous studies and of the working hypotheses. The findings and their implications should be discussed in the broadest context possible. Future research directions may also be highlighted.

3.1. Extraction of Microscopic Pore Images Based on Fuzzy Clustering. Fuzzy clustering is a dynamic iterative clustering algorithm used for segmentation, compression, and recognition of medical images. Thus, a SEM pore image is extracted using fuzzy clustering for the indoor microscopic test, dividing it into five classes. The darkest image adaptively serves as the pore image, which is then subjected to binarization to obtain a binary image and to compute the microscopic parameters of mechanical response. The principle of the fuzzy clustering algorithm is the minimization of the target function, where data and measurement similarities are clustered. The target function is shown in the following equation:

$$J_m = \sum_{i=1}^{N} \sum_{j=1}^{C} u_{ij}^m \left\| x_i - c_j \right\|^2, \quad 1 \le m \le \infty, \tag{1}$$

where m is the real number greater than 1, u_{ij}^m is the degree of membership of x_i in j, x_i is the d-dimensional data of the ith measurement value, c_j is the center of clustering of the jth class, and $\|*\|$ represents the similarity of any measurement vector to the clustering center.

The steps of the fuzzy clustering algorithm are as follows:

Step 1. Initialize the membership matrix, $U = [u_{ij}]$, $U^{(0)}$:

$$u_{ij} = \frac{1}{\sum_{k=1}^{C} \left(\left\| x_i - c_j \right\| / \left\| x_i - c_k \right\| \right)^{1/m-1}}. \tag{2}$$

Step 2. Compute the weight clustering central vector, c_j:

$$c_j = \frac{\sum_{i=1}^{N} u_{ij}^m x_i}{\sum_{i=1}^{N} u_{ij}^m}. \tag{3}$$

Step 3. Update the membership matrix, $U^{(k)}$, U^{k+1}. Stop iteration if $\|U^{k+1} - U^{(k)}\| < \varepsilon$; otherwise, return to Step 2.

This experiment uses five SEM images having the different CPB curing times mentioned above. The pore images are extracted using fuzzy clustering. The SEM images are divided into five clusters (i.e. "bright," "fairly bright," "fairly dark," "dark," and "darkest"). The darkest extracted image selected from the clustering is the pore image. The parameters of the specific clustering algorithm are $m = 2$; $j = 5$; c_j is the jth cluster center; x_i is the gray value of the gray level image; and ε is the iterative error. The fuzzy clustering method is used for classification, as shown in Figure 3. The figure presents the SEM image of the CPB at 56 d after curing age. Figure 3(a) is

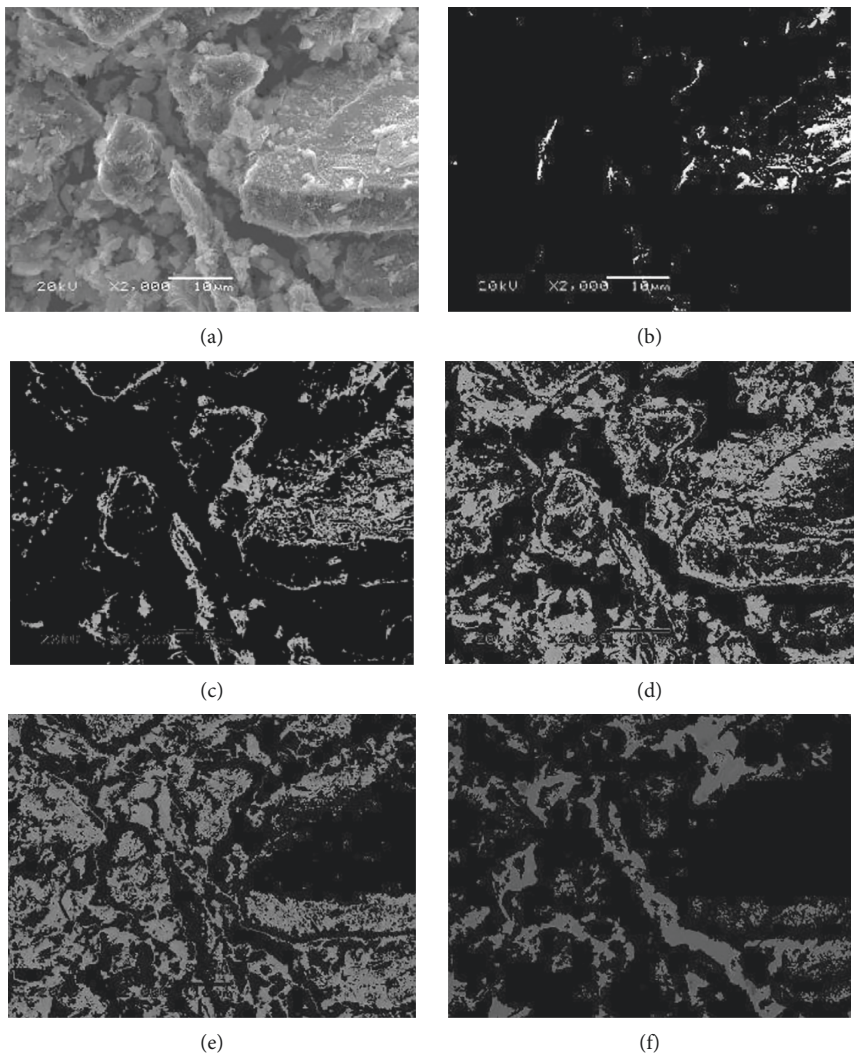

Figure 3: Clustering result of the pore image for CPB, based on fuzzy clustering. (a) Original image. (b) Bright. (c) Fairly bright. (d) Fairly dark. (e) Dark. (f) Darkest.

the original image, and Figures 3(b)–3(f) are the five states of the clustering image. In Figure 3(f), the image objectively reflects the distribution of pores on a microscopic scale. Thus, it serves as the pore image.

3.1.1. Extraction of Pore Images. As can be seen from Figure 3(f), there are various point regions. To extract the accurate pore region, small regions of less than 40 pixels are removed as noise during software processing. The remaining regions are then used as inverted binary pore images. The tiny image connection points are thus removed morphologically. Figure 4 presents the binary image with the miscellaneous point regions removed. The SEM images are presented with pores after 3, 7, 14, 28, and 56 days of curing time.

3.2. Quantitative Analysis of Pore Parameters. The pore images are extracted from the SEM CPB image to quantitatively describe the mechanical response and microscopic pore characteristics (e.g., distribution, quantity, direction, and size). The microscopic parameters include the region number, total region area, average length, pore porosity, uniformity coefficient, curvature coefficient, sorting coefficient, fractal dimension, weighted probability entropy, maximum region area, and average region area. As per the morphological and geometrical characteristics of the binary images, the following microscopic CPB indexes are proposed for the quantitative pore analysis:

(1) Region number reflects the number and sizes of pores on the image.

(2) Total region area is the sum of the total areas of all pores.

(3) Average length is the Feret diameter, which is used to define the length of a region.

(4) Pore porosity reflects the integrity of CPB pores and is the ratio of the pore region to the total image area. It is a 2D parameter indirectly reflecting the changes of the pore ratio in 3D space.

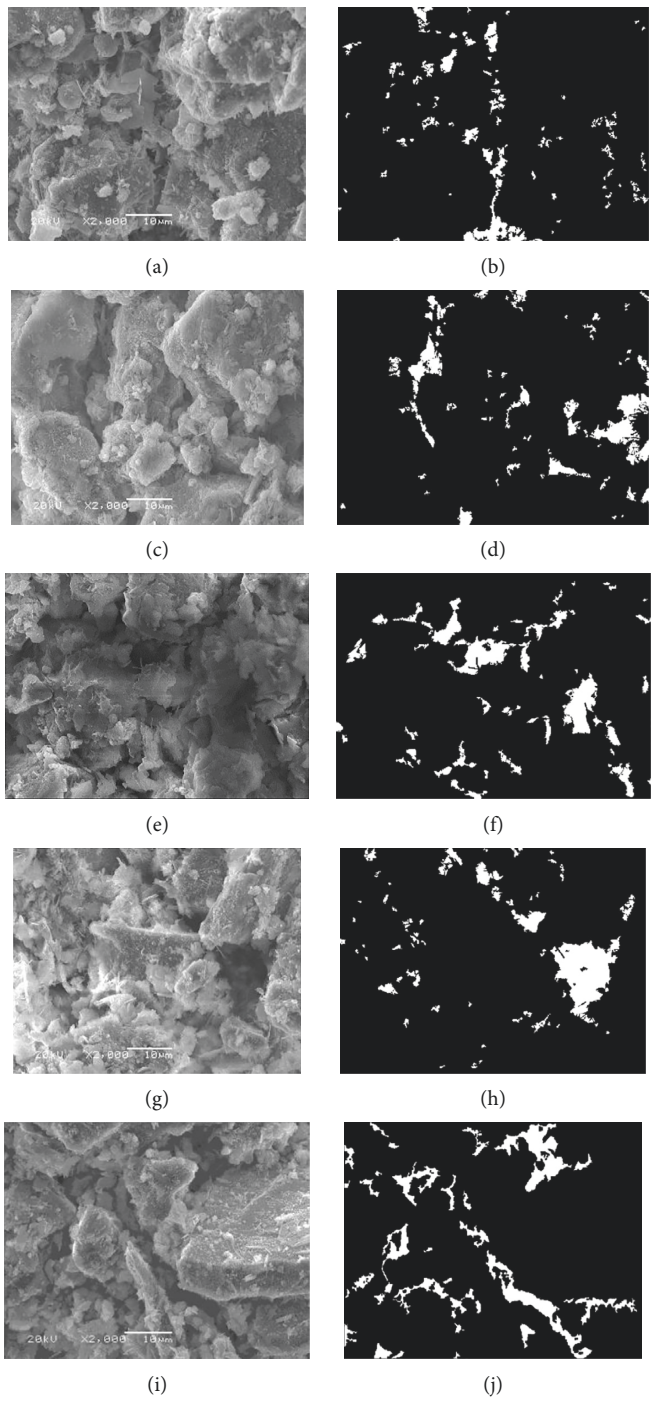

Figure 4: SEM images and corresponding binary pore images after different curing times. (a) Original image (3 d); (b) binary image of pores. (c) Original image (7 d); (d) binary image of pores. (e) Original image (14 d); (f) binary image of pores. (g) Original image (28 d); (h) binary image of pores. (i) Original image (56 d); (j) binary image of pores.

(5) Uniformity coefficient, C_u, is the ratio of d_{60} to d_{10}:

$$C_u = \frac{d_{60}}{d_{10}}, \tag{4}$$

where d_{10} is the diameter of the corresponding pore image block when the cumulative area is 10%. d_{60} is the diameter of the corresponding pore image block when the cumulative area is 60%.

(6) The curvature coefficient reflects whether the cumulative curve for the diameter of the pore image block is continuous:

$$C_c = \frac{d_{30}^2}{(d_{60} * d_{10})}, \tag{5}$$

where d_{10} and d_{60} are equal to the uniformity coefficient, C_u. d_{30} is the diameter of the corresponding pore image block when the cumulative area is 30%.

(7) Sorting coefficient, S_c, is used to sort the pore image blocks in descending order by area. When the size of the pore area is uniform, the values, P_{25} and P_{75}, are very similar. Thus, S_c is closer to 1, the other is larger than 1:

$$S_c = \frac{p_{25}}{p_{75}}, \tag{6}$$

where d_{25} and d_{75} reflect the diameters of the pore image block corresponding to the cumulative pore areas of 25% and 75%, respectively.

(8) The fractal dimension of porosity [17] is the quantitative index used to describe the CPB size distribution. It directly reflects the changing pore shape. The cumulative number of pores smaller than a certain pore, r, where $N(\leq r)$, is used to describe pore shape distribution characteristics. Both have good power function correspondences. $N(\leq r) \propto r^{-D_c}$ and $N(\geq r) = M - N(\leq r)$, where M is the total number of pores and a constant, $N(\geq r)$, represents the number of pores with a diameter larger than a certain pore diameter. When M is fixed, $N(\leq r)$ and $N(\geq r)$ have a constant correspondence relationship. Thus, the relationship, $N(r) \propto r^{-D_c}$, is also considered to be true. D_c is defined as the fractal dimension of porosity. For specific computation, the pore diameter, r, serves as the abscissa, corresponding to the number of pores having a diameter larger than $N(r)$. The correspondence relationship is determined using the double logarithmic coordinate system. The negative value of curvature of the stable straight portion serves as the fractal dimension of porosity. The computation formula is

$$D_c = \frac{-\lim \ln N(r)}{\ln r}. \tag{7}$$

A larger fractal dimension of porosity, D_c, leads to a lower level of pore homogenization and a larger difference of size among pores.

In our experiment, the pore image was divided into small square grids. r of each grid is 1, 3, 5, 7, and so on. The maximum value of r is a quarter of the image width. $N(r)$ denotes the number of pores in a square grid corresponding to r.

(9) Weighted probability entropy is a quantitative parameter reflecting the regularity of structural units.

It describes the overall CPB arrangement of pores at a microscopic scale. For the distribution in each small region, the computational formula of probability entropy, h_m, is

$$h_m = -\sum_{i=1}^{n} p_i \log_n p_i, \tag{8}$$

where p_i is the frequency of a structural body in a certain directional region, n is the interval of the orientation angles in the arrangement direction of structural units, and the value of h_m is between 0 and 1. A larger h_m leads to a more disordered arrangement of pores and lower regularity, and vice versa. In the experiment, given that $n = 36$, every 10° is a sector. The midpoint of the long axis of each pore is selected as the coordinate of the original point, with a horizontal x-axis and a vertical y-axis.

Owing to the size of each area block being different across the whole region, the contribution rate is also different. Thus, a new parameter is defined as the weighted probability entropy. All regional blocks on the pore image are subject to normalization, as shown in the following equation:

$$a_i = \frac{s_i}{\sum_{i=0}^{N-1} s_i}, \tag{9}$$

where there are N image blocks on the pore image, s_i represents the area of the ith region, and a_i represents the rate of contribution of the ith region following normalization and is regarded as the weighted value. The final weighted probability entropy is

$$H_m = \sum_{i=0}^{N-1} a_i h_{mi}, \tag{10}$$

where h_{mi} represents the probability entropy of the ith region and H_m represents the overall probability entropy of the pore image.

4. Analysis of Microscopic Parameters and Mechanical Responses of Pores

TensorFlow is a deep learning framework developed by Google. In the experimental stage, a TensorFlow framework is established to predict the mechanical strength based on multiple microscopic parameters. First, a TensorFlow framework is established. Second, multiple microscopic parameters are computed. Finally, the TensorFlow network is trained and tested to predict the mechanical CPB strength.

4.1. Construction of the TensorFlow Network. The framework comprises a basic neural network structure, an input layer, a hidden layer, and an output layer. As shown in Figure 5, the TensorFlow structure is established during the training stage. The network structure comprises 11 input nodes, 10 hidden nodes, and one output node. The output nodes are 11 microscopic parameters, and one output node is the mechanical response strength.

The network includes input layer, hidden layer, and output layer. A part of the code is given below:

Defined hidden layer:

```
weights_l1=tf.Variable(tf.random_normal([11,10]))
Biases_l1=tf.Variable(tf.zeros([11,10]))
wx_plust_b_l1=tf.matmul(x,weights_l1)+biases_l1
l1=tf.nn.tanh(wx_plust_b_l1)
```

Defined output layer:

```
weights_l2=tf.Variable(tf.random_normal([10,1]))
Biases_l2=tf.Variable(tf.zeros([1,1]))
wx_plust_b_l2=tf.matmul(l1,weights_l2)+biases_l2
prediction=tf.nn.tanh(wx_plust_b_l2)
```

Loss function:

```
Loss=tf.reduce_mean(tf.square(y-prediction))
```

Defined loss function expression:

$$\mathrm{MAE}(y, \hat{y}) = \frac{1}{n_{\text{sample}}} \sum_{i=1}^{n} (y_i - \hat{y}_i)^2. \tag{11}$$

4.2. Computation of Microscopic Parameters. The nonlinear relationship between the microscopic parameters and the mechanical response is described in this section.

(1) Digital processing software is used to analyze the CPB's SEM and to obtain relevant microscopic parameters, as shown in Table 3. The table presents 11 2D microscopic parameters.

(2) The maximum value, $x_{\max}$, and the minimum value, $x_{\min}$, of each parameter were obtained in the sample and processed via the dimensionless method. The parameter ranges are 0.1~1.1, and the equation is as follows:

$$x_t = \frac{x - x_{\min}}{x_{\max} - x_{\min}} + 0.1. \tag{12}$$

Figure 6 represents the uniaxial compressive strength of the CPB at 3, 7, 14, 28, and 56 days after curing. The uniaxial compressive strength increases with the period because both share a positive correlation.

4.3. Prediction Model. A prediction mode having 11 nodes and 11 microscopic parameters for the input layer is built in this experiment. The hidden layer has 10 nodes. The output layer has 1 node (i.e., mechanical response). The microscopic parameters are extracted from the pore image at 3, 7, 14, 28, and 56 days after model creation. 10 sets are used for each pore image. There are 50 training sample sets. Each sample set comprises 11 microscopic parameters. 20 prediction sample sets are used in the test stage after completion of TensorFlow network training. The mechanical response strength of the prediction samples and the test response are compared. Table 4 presents a comparison between the mechanical response and test strength of the prediction samples and the test of a sample set. Furthermore, two parameters are subject to

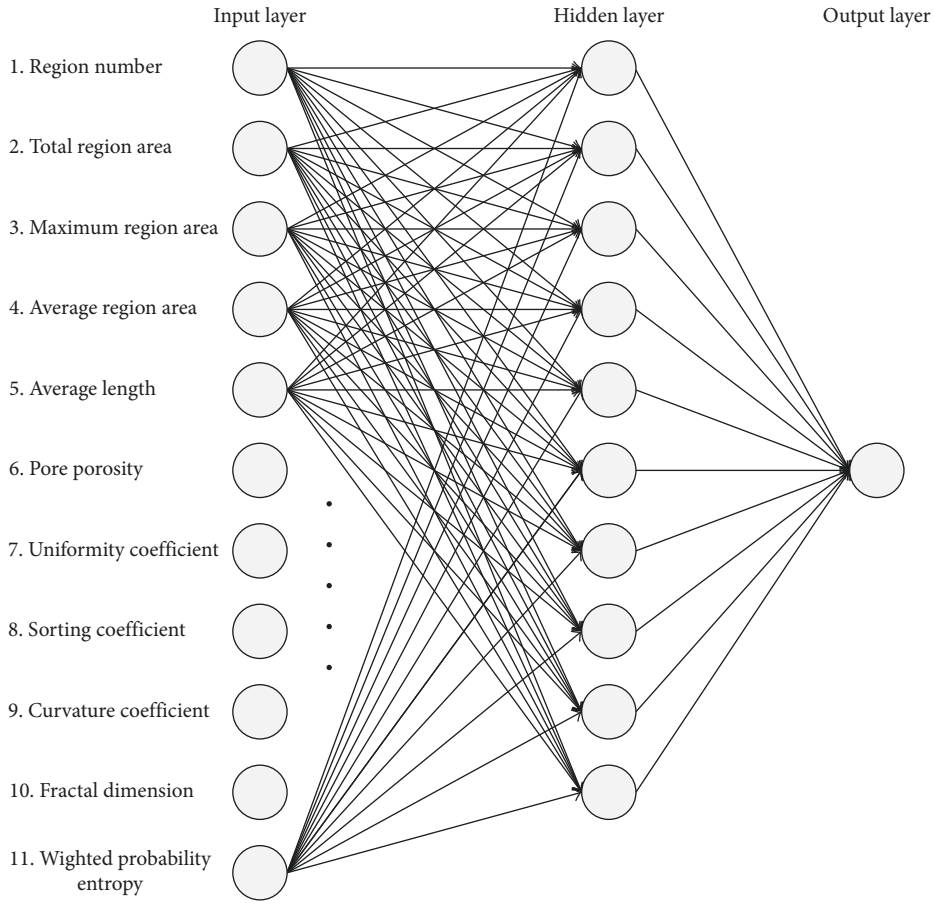

Figure 5: Three-layer TensorFlow structure.

Table 3: Microscopic parameters.

Number	Microparameters	Curing time				
		3 d	7 d	14 d	28 d	56 d
1	Image area	1228800	1228800	1228800	1228800	1228800
2	Region number	150	101	146	116	109
3	Total region area	78938	76767	55399	54249	49731
4	Maximum region area	9575	14595	7619	5852	5228
5	Average region area	526.25	760.07	379.45	467.66	456.25
6	Average length	33.03	41.29	29.64	32.35	33.4
7	Porosity	0.0642	0.0625	0.0451	0.0441	0.0405
8	Uniformity coefficient	1.531558	1.753211	1.520978	1.563739	1.536875
9	Sorting coefficient	1.324088	1.201636	1.526259	1.375541	1.333298
10	Curvature coefficient	1.082975	1.394743	0.969289	1.046084	1.071773
11	Fractal dimension	1.2178	1.274	1.2157	0.2606	1.2752
12	Weighted probability entropy	0.9778	0.9557	1.6391	0.9591	0.9541

error analysis. The predicted strength, s_p, and the actual strength, s_f, are subject to accuracy analysis:

$$a = \frac{\sum_{i=1}^{N} \left| s_{pi} - s_{fi} \right|}{\sum_{i=1}^{N} s_{fi}} * 100\%. \quad (13)$$

An error function is defined as follows:

$$e = \left| s_p - s_f \right|. \quad (14)$$

The analysis of the 40 sets of error statistics is shown in Table 5. The error statistical index is an average value of error, minimum and maximum of error, standard deviation of error, and accuracy. The average value of error is 0.0867 mPa, minimum value is 0.021, maximum value is 0.203, standard deviation is 0.0786, and error is 9.51%. The proposed method is compared with the traditional back propagation (BP) network for precision prediction [17]. The error is 21.95% by the traditional BP network.

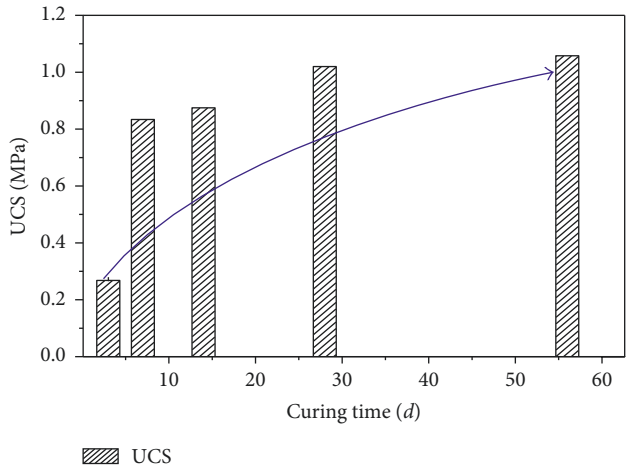

Figure 6: Uniaxial CPB compressive strength at different curing times.

Table 4: Comparison of predicted and tested sample strengths.

Number	Curing time	Actual strength, s_f (MPa)	Predicted strength, s_p (MPa)
1	3 d	0.268	0.247
2	7 d	0.834	0.782
3	14 d	0.875	0.815
4	28 d	1.02	0.975
5	56 d	1.058	1.112

Table 5: The statistical index of the error for mechanical strength.

Average value of error	Minimum value of error	Maximum value of error	Standard deviation of error	Error
0.0867	0.021	0.203	0.0786	9.51%

5. Conclusion

This paper established computer vision intelligent recognition of digital pore images as per the geometrical characteristics and morphological structure of the CPB and proposed a series of measurement indexes (i.e., region number, total region area, average length, pore porosity, uniformity coefficient, curvature coefficient, sorting coefficient, fractal dimension, weighted probability entropy, maximum region area, and average region area) for the quantitative analysis. This process reduced the human error and objectively reflected the CPB's microscopic structure. Google's TensorFlow deep learning architecture was used to establish the nonlinear relationship between 11 microscopic parameters and CPB's mechanical response. To effectively represent the orientation of the pores, the concept of weighted probability entropy was proposed, as were the contribution rates of different image regions. This digital image processing technique provided an effective method for the quantitative analysis of CPB pores, which achieved a good quantitative pore result. The method can predict the approximate strength of the cemented paste backfill based on the microscopic parameters obtained by processing the SEM image. The predicted average error is 9.51%. The accuracy of the proposed method is higher than that of the traditional method. A 2D image analysis technique is further developed for CPB, thus allowing more accurate and comprehensive analyses of CPB. By using this simple method, the microscopic structure of CPB is objectively characterized without rich and professional background and experience, which does not require a lot of manpower, material, and financial resources and guide the experiment process effectively.

Data Availability

The data used to support the findings of this study are available from the corresponding author upon request.

Conflicts of Interest

The authors declare that there are no conflicts of interest regarding the publication of this paper.

Authors' Contributions

Xuebin Qin and Pai Wang conceived and designed the experiments; Lang Liu and Mei Wang performed the experiments; Jie Xin analyzed the data; Lang Liu contributed SEM image; and Xuebin Qin wrote the paper.

Acknowledgments

This research was supported by the National Natural Science Foundation of China (nos. 51704229, 51504182, 51674188, 51404191, and 51405381), the Natural Science Basic Research Plan of Shaanxi Province of China (no. 2015JQ5187), the Scientific Research Program funded by the Shaanxi Provincial Education Department (nos. 15JK1466 and 15JK1472), the Project funded by China Postdoctoral Science Foundation (no. 2015M582685), and the Industrial Science and Technology Research Foundation of Shaanxi Province (no. 2016GY040).

References

[1] G. Deqing, S. Mengfei, S. Guanghua, L. Zhiyi, and H. Shuiqing, "Analysis of strength characteristics of cemented tailings backfill in high altitudes," *Chemical Minerals and Processing*, vol. 11, no. 4, pp. 46–48, 2016.

[2] L. Xin and W. Bingwen, "Study on mechanical properties and microstructure of the cemented tailings backfill," *China Mining Magazine*, vol. 25, no. 6, pp. 169–172, 2016.

[3] Z. Qinli, L. Xieping, and Y. Wei, "Optimization of filling slurry ratio in a mine based on back-propagation neural network," *Journal of Central South University*, vol. 44, no. 7, pp. 2867–2874, 2013.

[4] F. Jianxin, D. Cuifeng, and S. Weidong, "Strength sensitivity and failure mechanism of full tailings cemented backfills," *Journal of University of Science and Technology*, vol. 36, no. 9, pp. 1149–1157, 2014.

[5] M. Fall, J. C. Célestin, and M. Pokharel, "A contribution to understanding the effects of curing temperature on the

mechanical properties of mine cemented tailings backfill," *Engineering Geology*, vol. 114, no. 3-4, pp. 397–413, 2010.

[6] X. Wenbin, W. Yunmin, D. Peng, Y. Tianjun, and Z. Tong, "Precursors to compression failure of cemented backfill mass based on the multiparameter method," *Rock and Soil Mechanics*, vol. 37, no. 2, pp. 399–406, 2016.

[7] X. Wenbin, T. Xichun, and Q. Yu, "Experiment of the resistivity characteristic of cemented backfill mass during the whole consolidation process," *Journal of China University of Mining and Technology*, vol. 46, no. 2, pp. 265–272, 2017.

[8] A. Ghirian and M. Fall, "Coupled behavior of cemented paste backfill at early ages," *Geotechnical and Geological Engineering*, vol. 33, no. 5, pp. 1141–1166, 2015.

[9] W. Sun, K. Hou, and Z. Yang, "X-ray CT three-dimensional reconstruction and discrete element analysis of the cement paste backfill pore structure under uniaxial compression," *Construction and Building Materials*, vol. 138, no. 1, pp. 69–78, 2017.

[10] G. Xiu, W. Dang, and Z. Liu, "Microstructure test and macro size effect on the stability of cemented tailings backfill," *International Journal of Digital Content Technology and Its Applications*, vol. 6, no. 14, pp. 387–397, 2012.

[11] C. Liu, B. Shi, and J. Zhou, "Quantification and characterization of microporosity by image processing, geometric measurement and statistical methods: application on SEM images of clay materials," *Applied Clay Science*, vol. 54, no. 1, pp. 97–106, 2011.

[12] C. Liu, C.-S. Tang, and B. Shi, "Automatic quantification of crack patterns by image processing," *Computer and Geosciences*, vol. 57, no. 2, pp. 77–80, 2013.

[13] S. Ouellet and M. Benzaazoua, "Characterization of cemented paste backfill pore structure using SEM and IA analysis," *Bulletin of Engineering Geology and the Environment*, vol. 67, no. 2, pp. 139–152, 2008.

[14] A. M. Diab, H. E. Elyamany, A. E. M. A. Elmoaty, and A. H. Shalan, "Prediction of concrete compressive strength due to long term sulfate attack using neural network," *Alexandria Engineering Journal*, vol. 53, no. 3, pp. 627–642, 2014.

[15] L. Zhang, K. Wu, Y. Zhong, and P. Li, "A new sub-pixel mapping algorithm based on a BP neural network with an observation model," *Neurocomputing*, vol. 71, no. 10–12, pp. 2046–2054, 2008.

[16] F. Momeni, D. J. Armaghani, M. Hajihassani, and M. F. M. Amin, "Prediction of uniaxial compressive strength of rock samples using hybrid particle swarm optimization-based artificial neural networks," *Measurement*, vol. 60, pp. 50–63, 2015.

[17] N. Nistico, F. Pallini, T. Rousakis, Y.-F. Wu, and A. Karabinis, "Peak strength and ultimate strain prediction for FRP confined square and circular concrete sections," *Composites Part B: Engineering*, vol. 67, pp. 543–554, 2014.